RADIO SCIENCE, VOL. 38, NO. 3, 8044, doi:10.1029/2002RS002750, 2003

About the effects of instrument errors in interferometric radiometry

Eric Anterrieu

Centre Européan de Recherche et de Formation Avancées en Calcul Scientifique, Signal and Image Processing, Toulouse, France

Philippe Waldteufel

Institut Piere Simon Laplace, Service d'Aéronomie du Centre National de la Recherche Scientifique (CNRS), Verrières le Buisson, France

Gérard Caudal

IPSL, Centre d'Etude des Environnements Terrestre et Planétaires, Vélizy, France

Received 18 July 2002; accepted 10 September 2002; published 8 February 2003.

[1] The SMOS mission is a European Space Agency (ESA) project aimed at global monitoring of surface soil moisture and sea surface salinity from radiometric L-band observations. The radiometer onboard SMOS uses a 2-D synthetic aperture concept in order to achieve satisfactory spatial resolution performances for a minimal cost in terms of payload mass and volume. As the satellite moves ahead, every area on Earth's surface is seen at a variety of incidence angles. This multiangular capability is used in the retrieval of geophysical parameters. A major issue for obtaining useful measurements of the surface salinity is the radiometric accuracy, since the overall dynamic range resulting from ocean salinity variations only extends over a few Kelvin. To improve instrument performances, it is foreseen that independent retrieved salinity estimates will be averaged over a suitable space/time domain. This should bring random uncertainties due to radiometric sensitivity down to around 0.1 Practical Salinity Scale (PSS). However, several systematic error sources are also present: biases arise from channel or baseline instrument errors and are superimposed to Gibbs oscillations generated through the reconstruction of brightness temperature fields from correlation products. It is thus of importance to assess to which extent these errors can be averaged out when building space/time averages of the retrieved salinity values. The presents study is a step toward addressing this issue. *INDEX TERMS:* 6969 Radio Science: Remote sensing; 6924 Radio Science: interferometry; 6994 Radio Science: Instruments and techniques; *KEYWORDS:* interferometry, radiometry

Citation: Anterrieu, E., P. Waldteufel, and G. Caudal, About the effects of instrument errors in interferometric radiometry, *Radio Sci.*, *38*(3), 8044, doi:10.1029/2002RS002750, 2003.

1. Introduction

[2] The SMOS mission, currently undergoing a phase B study, is an European Space Agency (ESA) led project aimed at global monitoring of surface soil moisture and sea surface salinity from radiometric L-band observations [*Kerr et al.*, 2001]. The radiometer on board SMOS is derived from MIRAS studies carried out by ESA; it uses a 2-D synthetic aperture (interferometric) concept in order to achieve satisfactory spatial resolution performances for a minimal cost in terms of payload mass and volume. One counterpart of this advantage is an increased intrinsic complexity of the instrument as well as data processing.

[3] The interferometer includes a large number of independent (ideally identical) channels, consisting of an elementary antenna having a large beam width and a receiver. Each pair of antennas defines an interferometric baseline, depending on their respective locations. For each baseline, correlation products are computed from signals provided at the output of both concerned

Copyright 2003 by the American Geophysical Union.
0048-6604/03/2002RS002750

receivers. These data are later processed and used in order to reconstruct the field of incident brightness temperatures over the solid angle accessible to the antennas.

[4] As the satellite moves ahead, every area on Earth's surface is seen at a variety of incidence angles. The principle for the retrieval of physical parameters consists in fitting model computed brightness temperatures to the radiometric (dual polarization) observations, over the range of available incidence angles.

[5] Over the open ocean, a major issue for obtaining useful measurements of the surface salinity is the radiometric accuracy, since the overall dynamic range due to salinity variations only extends over a few Kelvin. While random salinity uncertainties, mostly due to radiometric sensitivity, are quite large when considering a single measurement, it is foreseen that independent retrieved estimates will be averaged over a sizable space/time domain: e.g., 200 $\times$ 200 km^2, 10 days, according to Global Ocean Data Assimilation Experiment (GODAE) requirements. This should bring this type of error down, enabling to achieve retrieval uncertainties better than 0.1 on the Practical Salinity Scale (PSS) [*Waldteufel et al.*, 2003].

[6] However, the synthetic aperture radiometer will also be specifically affected by several nonrandom errors. Such errors may be first be sorted out in two categories [*Camps*, 1996]:

1. Imperfect knowledge of properties of the antenna and receiver associated to each element of the interferometer gives rise to antenna and ''channel'' errors.
2. Imperfect knowledge of receiver subsystems used for building correlation products and resultant visibility functions from signals yielded by each pair of channels gives rise to ''baseline'' errors.

[7] In addition, Gibbs oscillations are generated by sharp gradients due to alias boundaries and the finite extent of the domain available for carrying out the reconstruction of the brightness temperature field from interferometric data.

[8] While there is little doubt that space/time averaging will be efficient in reducing the random error on the salinity measurements, the answer is not straightforward for systematic errors. This is a significant issue, since overall inaccuracies resulting from such errors have been so far estimated to reach about 1 K [*Corbella et al.*, 2000a, 2000b], whereas the accuracy required for achieving salinity measurements to better than 0.1 PSS is estimated to be substantially less than 0.1 K.

[9] This paper reports the results of a numerical study that attempts to address this question. Receiver errors for the MIRAS radiometer have been analyzed in detail [*Torres et al.*, 1997] as well as antenna errors [*Camps et al.*, 1997b]; however the specific issue of averaging properties has not been investigated when considering the whole SMOS field of view (FOV), since only a small region centered on the antenna bore sight was considered in previous studies. It was indeed only recognized in the recent years that in order to exploit fully 2-D interferometric radiometry, it was appropriate to use the whole FOV of the instrument.

[10] In this approach, we consider many kinds of instrument errors; while it is not attempted to achieve exhaustivity, at least every major generic kind of error is represented. The simulation method is presented in section 2 while the simulation scenario and results obtained are detailed in section 3, which also considers the effect of averaging redundant visibility samples. In section 4, we present a numerical application to the SMOS mission and summarize the main conclusions.

2. Simulation Method

[11] While classical radiometers measure the power collected by a highly directive antenna, which is directly related to the brightness temperature in the main beam direction, interferometer measurements are obtained by cross-correlating the signals collected by pairs of non-directive antennas which have overlapping fields of view, giving samples of the so-called visibility function. Neglecting the fringe wash effects due to the finite bandwidth of the receivers, the relation between the brightness temperature T and the visibility samples V is given by [*Ruf et al.*, 1998; *Bara et al.*, 1998]:

$$V_{kl} \equiv V(u_{kl}, v_{kl}) \propto \frac{1}{\sqrt{\Omega_k \Omega_l}} \iint\limits_{\xi^2+\eta^2 \le 1} F_k(\xi,\eta) F_l^*(\xi,\eta) \cdot T(\xi,\eta) e^{-2j\pi(u_{kl}\xi + v_{kl}\eta)\frac{d\xi d\eta}{\sqrt{1-\xi^2-\eta^2}}} \quad (1)$$

where (u_{kl}, v_{kl}) are the components of the baseline vector from antenna k to antenna l; F_k and F_l are the normalized (complex) antenna voltage patterns (Ω_k and Ω_l are the equivalent solid angle of these antennas). The current variables $\xi = \sin\theta\cos\phi$ and $\eta = \sin\theta\sin\phi$ are direction cosines with respect to an orthogonal frame attached to the center of the interferometric array.

[12] The basic settings of the instrument are close to the baseline configuration selected for SMOS: a Y-shaped array with 21 antennas per arm equispaced 0.875 λ, plus the central one; antenna patterns are axisymmetrical and representative of those designed for SMOS. The full model [*Waldteufel and Caudal*, 2002], includes a simple dependence of the voltage gain with respect to the antenna elevation angle θ: $F = 1 - 0.95\ \sin(\theta)^{1.9}$. The full width at half maximum value (FWHM) is then equal to $2\ \mathrm{asin}(1.9)^{-1/1.9} \approx 91°$.

[13] The antenna plane is viewing the Earth from an elevation of 800 km above the Earth's surface, with a tilt angle of 30° above the horizontal plane. The initial

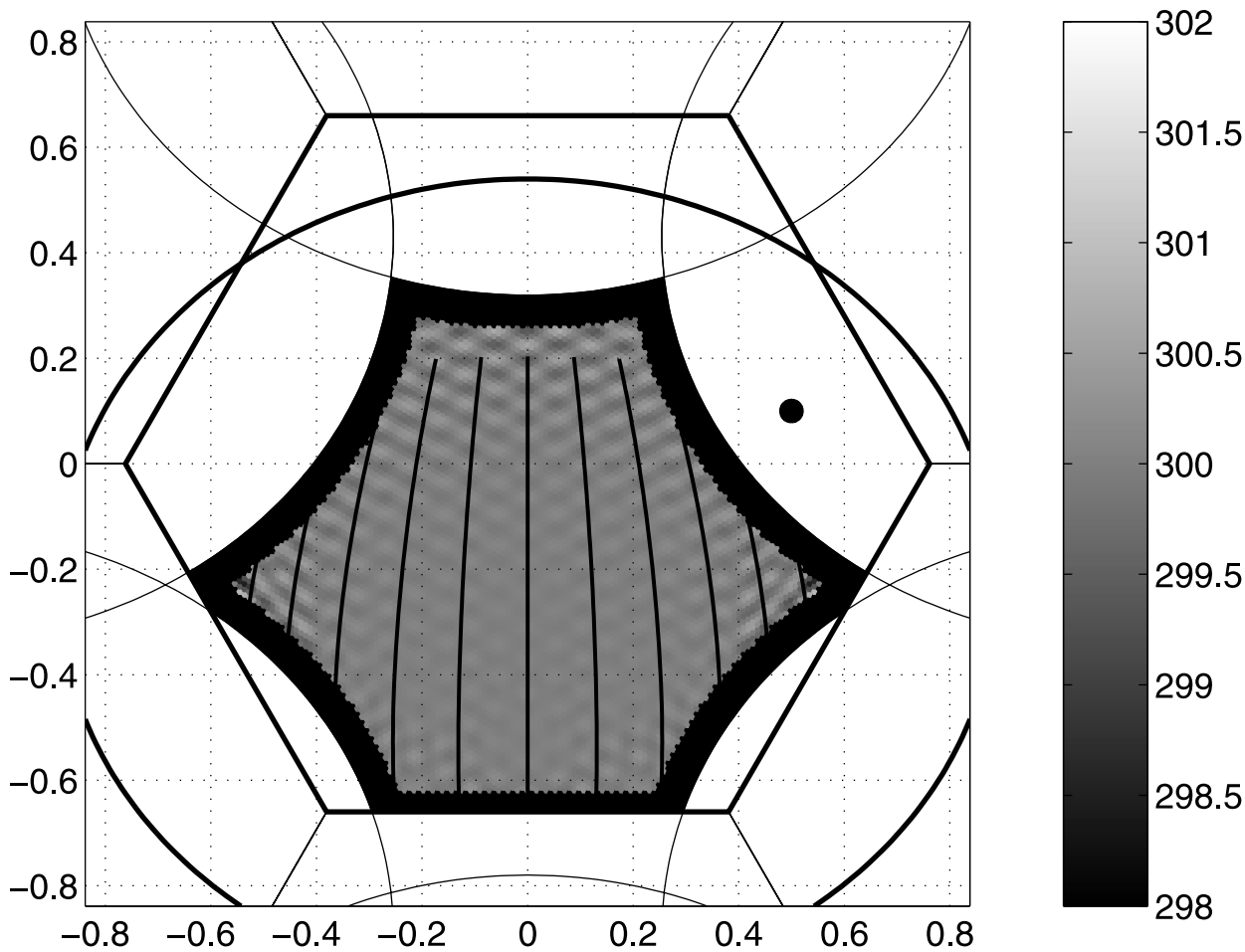


Figure 1. (a) Reconstructed image of a 300 K homogeneous target in the SMOS FOV showing Gibbs oscillations, for a 30° tilting angle of the antenna plane and a 30° steering angle of the Y-shaped interferometer, in the frame of direction cosines. The alias-free FOV is limited by replicas of the Earth horizon (blue ellipses). Also shown are the margins applied to the reconstruction zone and the limits between dwell lines for building the statistics (magenta lines are spaced 100 km apart). The width of the margins is 1.5 times the resolution provided by the half maximum Blackman window in the direction cosine frame (shown as a blue circle in the upper right part of the figure). (b) Histograms of the discretization error (K) for different dwell lines (violet) and for the whole FOV (green). In each case, the mean area bias and the area spread **m** and **a** are depicted (see text). See color version of this figure at back of this issue.

brightness temperature distribution corresponds to that of a flat field at 300 K over the Earth and 3.7 K over the cold sky.

[14] To simulate the signal measured by a 2-D interferometric radiometer, the modified visibilities $\widetilde{V}_{kl}$ are computed from the above mentioned temperature field, in a first (forward) step. To this end, imperfections in various parts of the interferometer are sequentially simulated through modifying or introducing factors in the right-hand side of (1).

[15] Selected antenna errors can affect the shape of each antenna voltage pattern, as well as its amplitude or phase. They can also be the consequence of effects that impact on the pointing accuracy of each radiating element:

$$\widetilde{F}_k(\xi,\eta) = F_k\left(\xi-\xi'_k,\eta-\eta'_k\right)(1+\rho_k(\xi,\eta))e^{\,j\alpha_k(\xi,\eta)} \quad (2)$$

where the α_k and the ρ_k are phase and amplitude errors for channel k, which may vary in the FOV of each

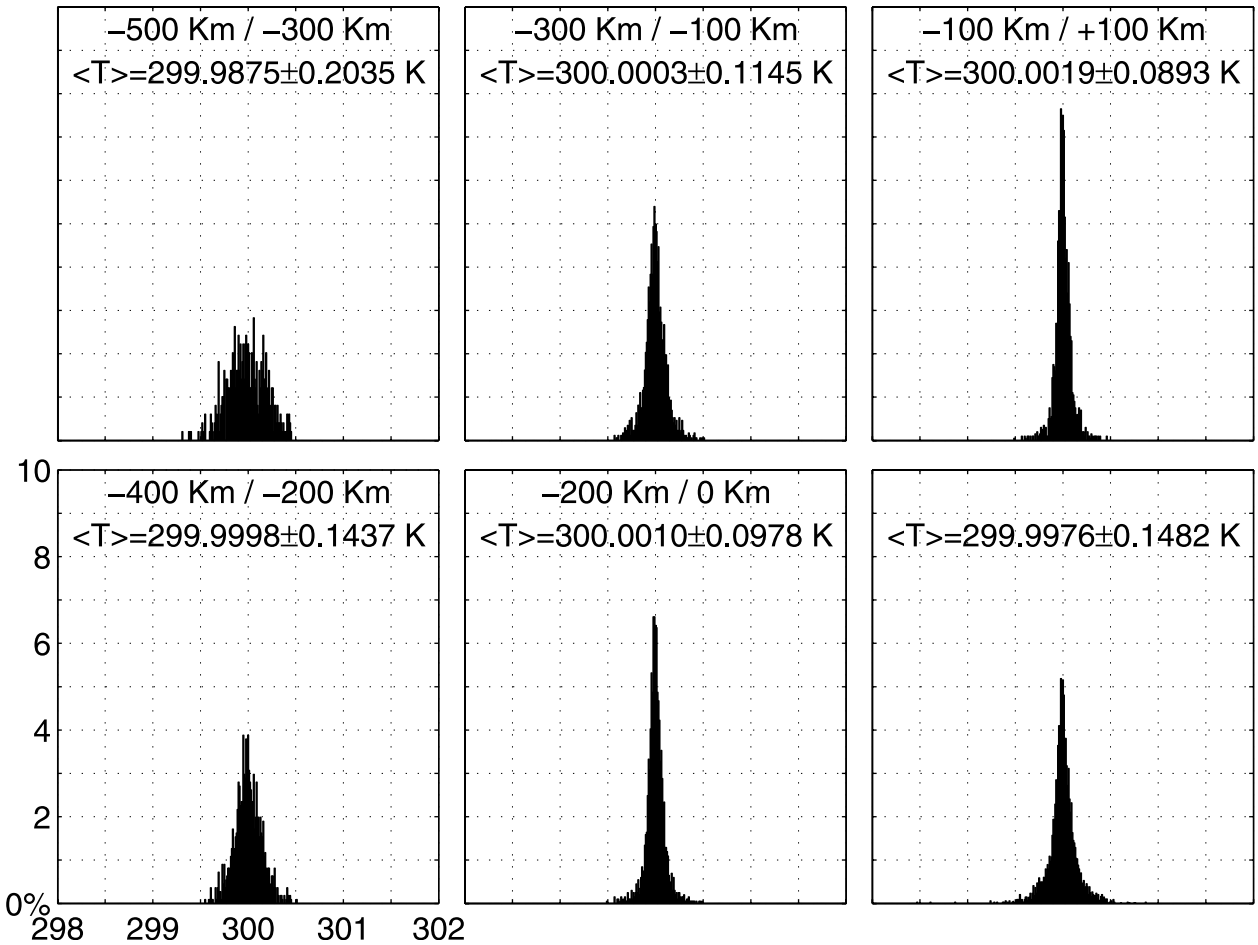


Figure 1. (continued)

antenna (and of course from one antenna to another), and the (ξ',η') are pointing errors with respect to the viewing direction.

[16] Receivers are affected by channel errors which may apply to either the amplitude or the phase, or both, of the complex visibility samples in a separable way:

$$\Re\mathrm{e}\left(\widetilde{V}_{kl}\right) = (1+g_k)(1+g_l)\Re\mathrm{e}\cdot\left(V_{kl}e^{-j\left(\varphi_k-\varphi_l+\frac{\psi_k-\psi_l}{2}\right)}\right)$$
$$\Im\mathrm{m}\left(\widetilde{V}_{kl}\right) = (1+g_k)(1+g_l)\Im\mathrm{m}\cdot\left(V_{kl}e^{-j\left(\varphi_k-\varphi_l+\frac{\psi_k+\psi_l}{2}\right)}\right) \quad (3)$$

where φ_k (resp. φ_l) are the in-phase errors for receiver k (resp. l), and ψ_k (resp. ψ_l) are the quadrature errors. The g coefficients are the amplitude errors (here expressed as fractions).

[17] Baseline (nonseparable) errors may affect either the amplitude, or the phase, or both, of the complex visibility samples. They are introduced through coefficients ε_{kl} and β_{kl}:

$$\widetilde{V}_{kl} = (1+\varepsilon_{kl})e^{j\beta_{kl}}V_{kl} \quad (4)$$

Similar approaches were followed by *Torres et al.* [1996] and *Torres et al.* [1997] for (3) and (4), respectively.

[18] The second (inverse) step consists of a basic reconstruction. It assumes a perfect instrument with identical antennas and receivers, thus providing output errors on reconstructed brightness temperatures which correspond to input errors introduced in the forward step; redundant visibility samples are averaged. As Y-shaped arrays consisting of equispaced antennas along each arm lead to visibility functions sampled over an hexagonal grid inside a star-shaped domain [*Lannes and Anterrieu*, 1994; *Camps et al.*, 1997a] apodization is required to filter out the effect of the sharp frequency cutoff. In this study, the exact Blackman window has been used to perform this. Finally,

Table 1. Statistics on Simulated Uniform Errors for Selected FOV Areas[a]

				Limits Across FOV (×100 km)						
	Nature of Error	Bias σ		(−6,−4)	(−4,−2)	(−2,0)	(0,2)	(2,4)	(4,6)	Whole FOV
	None	0	**m**	−0.06	0.00	0.00	0.00	0.00	−0.06	0.00
	(Gibbs)		**a**	0.35	0.14	0.10	0.10	0.14	0.35	0.15
1	Antenna	0.1°	**m**	−0.48	−0.54	−0.57	−0.57	−0.54	−0.48	−0.56
	FWHM		**a**	0.35	0.17	0.16	0.16	0.17	0.35	0.19
2	Antenna	1%	**m**	−1.15	0.16	0.47	0.47	0.16	−1.15	0.32
	Amplitude		**a**	0.74	0.99	1.32	1.32	0.99	0.74	1.23
3	Antenna	0.1°	**m**	−1.22	−0.68	−0.32	0.15	0.64	1.07	−0.04
	Pointing		**a**	0.41	0.36	0.37	0.30	0.24	0.35	0.60
4	Antenna	1°	**m**	−0.12	−0.01	0.02	−0.02	0.01	0.01	0.00
	Phase		**a**	0.35	0.15	0.11	0.11	0.15	0.35	0.16
5	Receiver	0.5%	**m**	0.46	−0.08	−0.22	−0.22	−0.08	0.47	−0.16
	Amplitude		**a**	0.40	0.50	0.64	0.64	0.50	0.40	0.60
6	Receiver	1°	**m**	−0.06	0.00	0.00	0.00	0.00	−0.06	0.00
	In-phase		**a**	0.35	0.14	0.10	0.10	0.14	0.35	0.15
7	Receiver	0.5°	**m**	−0.29	−0.55	−0.65	−0.33	−0.23	−0.17	−0.40
	Quad-phase		**a**	0.36	0.47	0.58	0.51	0.45	0.36	0.57
8	Baseline	2%	**m**	−1.16	0.16	0.47	0.47	0.16	−1.16	0.32
	Amplitude		**a**	0.75	1.01	1.35	1.35	1.01	0.75	1.26
9	Baseline	1°	**m**	0.57	1.15	1.26	0.62	0.50	0.32	0.79
	Phase		**a**	0.51	0.77	0.99	0.84	0.74	0.47	0.98

[a]Top of table: Gibbs errors: area averages **m** and area dispersions **a** (see text). Next: for each of the nine selected input errors labeled from 1 to 9, shown are area averages **m** and area spreads **a** of the output error (K) when the input error is an uniform bias of magnitude σ (standard deviation of the Gaussian distribution to be used later) applied to an uniform scene with T^0 = 300 K. The statistics are given in columns for selected strips 200 km wide across the FOV and for the whole area.

from the apodized $\widetilde{V}_{kl}$, erroneous $\widetilde{T}(\xi,\eta)$ are obtained through inverting (1).

3. Simulation Scenarios and Results

3.1. Discretization Errors and Selection of Areas on the FOV

[19] The simulations reported here are restricted to errors due to imperfect knowledge of the instrument. However, discretization errors are always present. They appear as a regular network of so-called Gibbs oscillations, which is displayed on Figure 1a.

[20] As Gibbs oscillations are generated by the sharp discontinuity near the limits of the alias-free FOV, their amplitude grows steeply when approaching these limits. This is one of the reasons for restricting the FOV with respect to its theoretical extent. Another one is attributable to the periodicity of the discrete Fourier transform, the elementary period being the hexagon shown on Figure 1a. Indeed, since the discrete Fourier transform assumes periodical functions in both spatial and Fourier domains, discontinuities at the edges of each period may also induce Gibbs oscillations. It was found adequate to retain a margin of the order of the half width of the apodization window, also shown on the figure.

[21] The figure also shows boundaries of zones inside the restricted FOV, for which individual statistics were built. These boundaries correspond to straight lines parallel to the satellite subtrack, spaced by 100 km; remember that for salinity estimation the SMOS data will be combined within such, 200 km wide, elongated zones or "strips."

[22] Corresponding area statistics are shown in the upper part of Table 1. Although results are given for the most remote strips which extend from ±400 to ±600 km away from the track, Figure 1 indicates that available areas beyond ±500 km are actually very small.

[23] Table 1 displays the area mean **m** and standard deviation **a** of the resulting output biases, computed as:

$$\mathbf{m} = \sum_n \left(T_n - T^0\right)/N; \quad \mathbf{a} = \sqrt{\sum_n \left(T_n - T^0\right)^2/N} \tag{5}$$

where T^0 is the input temperature field and summation is performed over the N pixels within considered FOV area.

[24] The magnitude of the area-averaged errors **m** is very small, since Gibbs oscillations are averaged when considering a significant number of reconstructed pixels. However, the spread **a** over each strip is significant, although lower in the center areas.

3.2. Constant Input Error

[25] Using formulations given above, we have selected nine kinds of input errors:

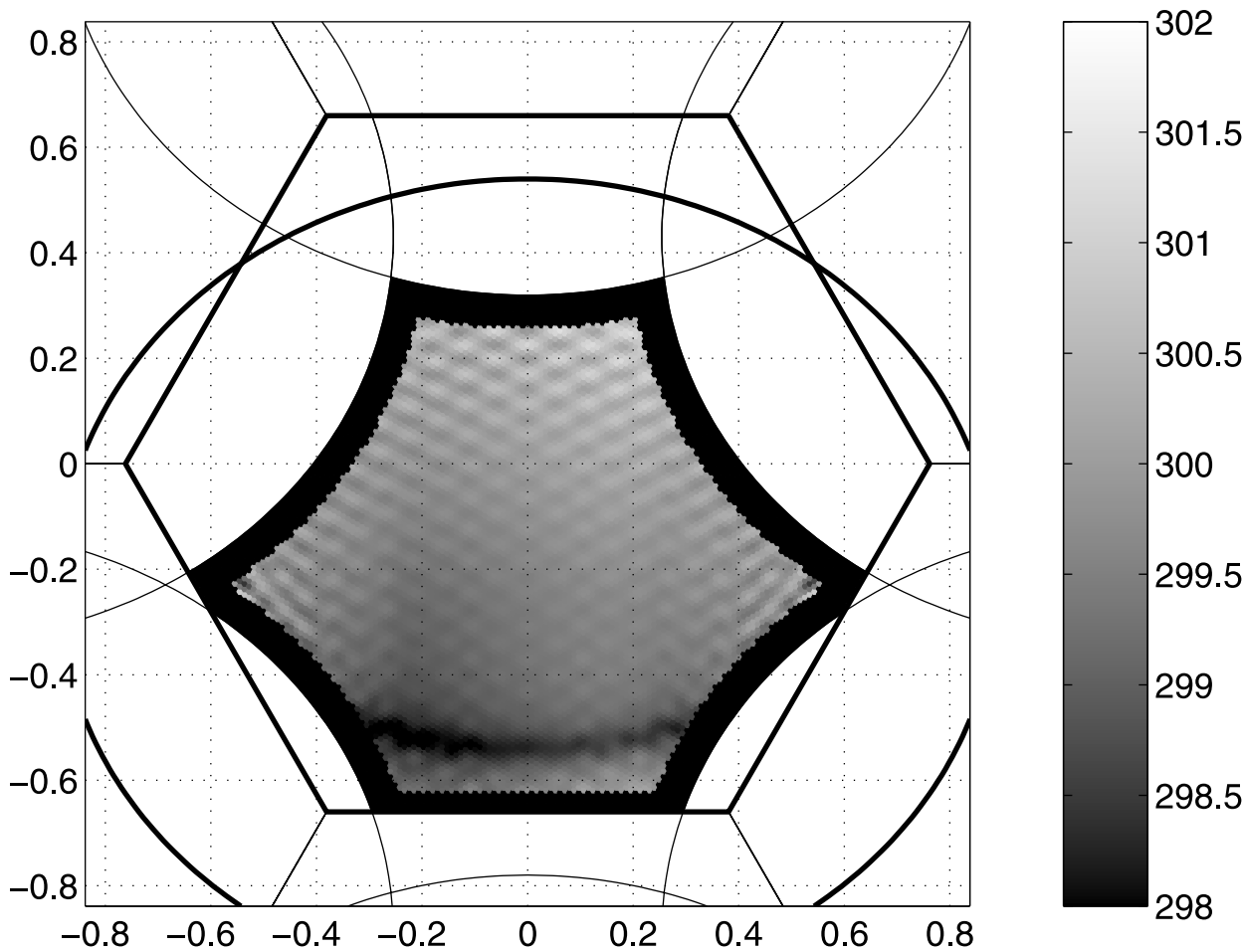


Figure 2. Same as Figure 1 when introducing a uniform 0.5° error on quadratic phases in the receiving channels (error case 7). See color version of this figure at back of this issue.

1. cases 1–4 (pattern width, voltage gain, pointing axis, and phase pattern) are related to the antenna patterns. The pattern width error is simulated as a modulation of the unperturbed pattern law (indicated in section 2 above); other errors are introduced in (2).

2. cases 5–7 (receiver amplitude, in phase and quadrature phase components) are meant to simulate receiver (channel) errors, and introduced in (3).

3. cases 8 and 9 (amplitude and phase) are applied to visibilities in (4) in order to simulate baseline errors.

[26] For each error parameter introduced in the above section, we specify in the forward calculation a constant input error σ, i.e., identical for every antenna, channel, or baseline. The magnitude of the bias σ is chosen empirically in order to obtain comparable magnitudes of errors in the reconstructed field. This computation was repeated for several σ values in order to verify the linearity of the response.

[27] Figure 2 illustrates (for case 7) the resulting errors when a uniform bias is introduced in the phase of the quadrature receiving channel.

[28] The values of **m** and **a** resulting from selected input errors for cases 1–9 are displayed in the lower part of Table 1. Since the magnitudes of input errors used for building the table are arbitrary, we shall not comment at length on the magnitude of output errors **m**. Note however that a constant in-phase receiver error (case 6 in Table 1) does not generate a bias: according to (3), the corresponding baseline phase error, which is of the form $(\varphi_k - \varphi_l)$, reduces to zero for every baseline when the φ's are constant. The particular choice of antenna phase errors (case 4) does not result

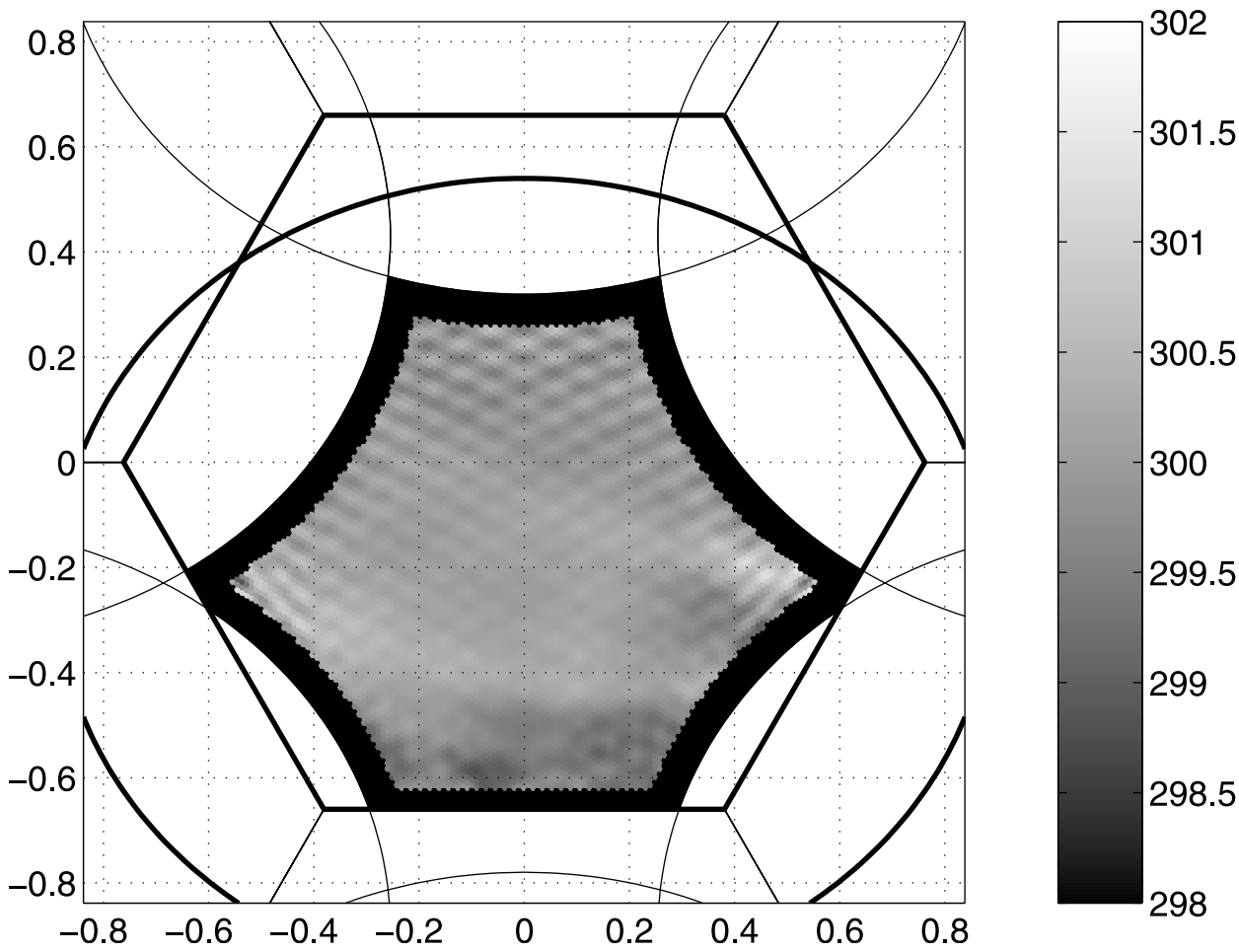


Figure 3. Errors on the reconstructed field when introducing a Gaussian distributed error with a 0.5° standard deviation on quadratic phases in the receiving channels (error case 7). (a) Example of reconstructed image, to be compared to Figure 2 (whole FOV) and (b) histogram of error values mapped on (a) (top part). The bottom part shows the successive values taken by **m** and **a** on the whole FOV when repeating the numerical experiment 100 times. The diagrams also display the building up of ensemble standard deviations **s(m)** and **s(a)** and show the resulting ensemble averages. See color version of this figure at back of this issue.

in an output bias either. In both cases, dispersions **a** are very close to the values induced by discretization phenomena alone.

[29] In the other cases, some reconstructed errors vary from one FOV strip to another. Amplitude errors (cases 1, 2, 5, and 8 in the table) generate a symmetrical structure; this is the case for neither phase errors (cases 7 and 9), nor the pointing error (case 3), which was expected. The only case where bias induced errors are homogeneous corresponds to the voltage pattern width (case 1). The area spread **a** follows a symmetry pattern across the FOV.

3.3. Random Input Errors: FOV Averaging

[30] Next, input errors are selected randomly for each antenna, channel, or baseline, out of a Gaussian population with standard deviation adjusted to the same σ value as above. Such trials are repeated P times, with P = 100, in order to allow the building of ensemble statistics.

[31] For each error type, 100 independent random distributions of input errors are then built, yielding area average errors $\mathbf{m_p}$ and standard deviations $\mathbf{a_p}$ for each trial **p** for the reconstructed field. Figure 3 illustrates the behavior of simulated results when input errors are

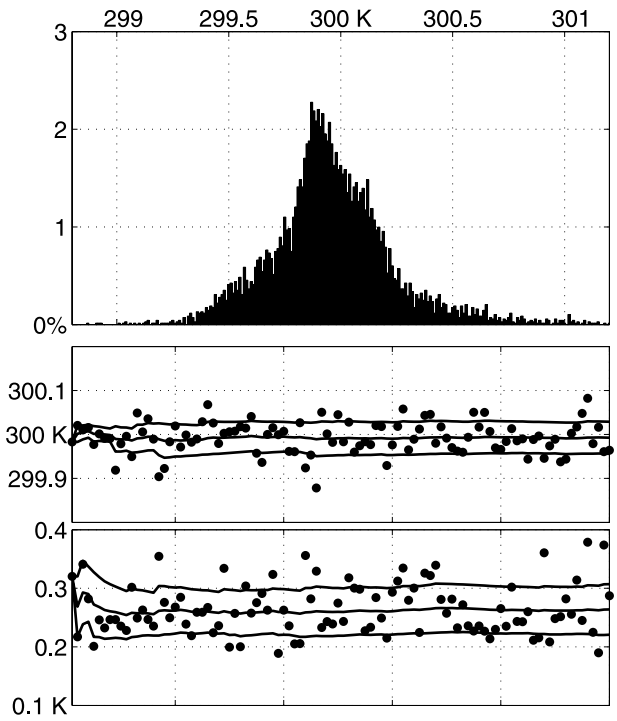


Figure 3. (continued)

randomized in this way, for the same conditions as for Figure 2.

[32] Ensemble averages $\langle \mathbf{m} \rangle$ and $\langle \mathbf{a} \rangle$, as well as standard deviations $\mathbf{s(m)}$ and $\mathbf{s(a)}$, are computed over populations of trials, according to:

$$\langle \mathbf{m} \rangle = \sum_p \mathbf{m_p}/\mathrm{P}; \mathbf{s}(\mathbf{m}) = \sqrt{\sum_p \left(\mathbf{m_p} - \langle \mathbf{m} \rangle\right)^2/\mathrm{P}}$$
$$\langle \mathbf{a} \rangle = \sum_p \mathbf{a_p}/\mathrm{P}; \mathbf{s}(\mathbf{a}) = \sqrt{\sum_p \left(\mathbf{a_p} - \langle \mathbf{a} \rangle\right)^2/\mathrm{P}} \quad (6)$$

The $\langle \mathbf{m} \rangle$ values are very small, as they are indeed expected to vanish when P becomes large; the $\mathbf{s(a)}$ figures range between 0.05 and 0.25 times the corresponding $\langle \mathbf{a} \rangle$ values.

[33] While the input error magnitudes considered so far are arbitrary, it is appropriate to consider the sensitivities of output errors to unit input errors. The resulting figures are shown on Table 2. The numerical application uses a 100 K target temperature, representative of open ocean; the error contributions have been scaled accordingly (excepting the residual channel amplitude error 5, which does not obey strict proportionality to target temperature, since it involves the scene temperature to receiver noise temperature ratio) [see *Torres et al.*, 1996].

[34] Since the ensemble spread $\mathbf{s(m)}$ of the area averages is representative of the magnitude of output errors affecting such averages, while the mean area spread $\langle \mathbf{a} \rangle$ is representative of output errors when no area averaging is carried out, Table 2 shows, for each error case and r.h.s. FOV strips, the sensitivities $\mathbf{R_r}$ and $\mathbf{R_{rm}}$ of $\langle \mathbf{a} \rangle$ and $\mathbf{s(m)}$ to unit input σ values. The reason for the subscript $\mathbf{r}$ is that redundant visibilities are averaged prior to reconstruction in the above simulations.

[35] We are interested in assessing the impact of averaging over the FOV the resulting output errors. To this end, it is relevant to compare the $\mathbf{R_{rm}}$ figures to the sensitivities $\mathbf{R_r}$ of the spread of output errors over the FOV, estimated by its ensemble average $\langle \mathbf{a} \rangle$.

[36] The obtained reduction factors can be understood as indicators of the way visibility errors are propagated to reconstructed brightness temperatures. These factors, although significant, are not very large; this may seem puzzling at first, when keeping in mind that errors on visibilities may be considered as randomly and uniformly distributed.

[37] We suggest that the reason for this is that output error structures are dominated by large scales, as illustrated by Figure 3a. This is due to the fact that, in the linear reconstruction operation, visibility errors appear in multiplying factors (which slightly differ from unity) rather than additive contributions; then, since the spectral power of the unperturbed (uniform) temperature field is concentrated at low spatial frequencies, the same trend is observed on output errors, which limits the efficiency of the area averaging procedure.

[38] The actual structure of the scene may have some impact on the resulting errors: an increased complexity should rather improve the situation as far as the propagation of instrument errors is concerned. However, ocean scenes will always appear as essentially homogeneous (since, due to the geometry of the measurement, the dependence of brightness temperatures on incidence angle is strongly reduced in fields collected by the antenna ports, as illustrated by *Waldteufel and Caudal* [2002]). Therefore, large-scale features due to the antenna voltage pattern will prevail in this case anyway.

3.4. Random Input Errors: Averaging Redundant Visibilities

[39] The predominance of large-scale errors in the temperature field, inasmuch as it corresponds to a predominance of contributions due to short baseline visibility terms, enhances the expected impact of redundancies. While the Y-shaped SMOS geometry was selected in order to minimize the fraction of redundant baselines (and indeed this fraction is circa 13%), redundancies still do occur for antenna elements paired along each arm, and mostly for the shortest baselines.

[40] In the simulations reported above, redundant visibilities were averaged before the reconstruction process. We have repeated every simulation reported above with-

Table 2. Sensitivities to Input Errors[a]

Case		Unit	Limits Across FOV (×100 km) (−1,1)	(0,2)	(1,3)	(2,4)	(3,5)	(4,6)	Whole FOV
1 Antenna Pattern Width	**R**	K/(°)	0.76	0.87	1.03	1.10	0.99	1.26	1.24
	$\mathbf{R_m}$		1.12	0.95	0.63	0.75	1.46	1.92	0.54
	$\mathbf{R_r}$		0.43	0.52	0.67	0.76	0.79	1.20	0.79
	$\mathbf{R_{rm}}$		0.42	0.32	0.21	0.46	0.82	0.94	0.15
	$\mathbf{R/R_{rm}}$		1.79	2.75	4.81	2.42	1.22	1.34	8.57
2 Antenna Voltage Gain	**R**	K/(%)	0.24	0.24	0.25	0.25	0.27	0.29	0.25
	$\mathbf{R_m}$		0.02	0.03	0.03	0.03	0.06	0.11	0.01
	$\mathbf{R_r}$		0.23	0.23	0.24	0.24	0.26	0.29	0.24
	$\mathbf{R_{rm}}$		0.01	0.02	0.02	0.03	0.05	0.09	0.01
	$\mathbf{R/R_{rm}}$		17.46	14.89	14.44	9.04	5.38	3.19	41.54
3 Antenna Pointing	**R**	K/(°)	1.17	1.17	1.14	1.09	0.97	1.25	1.40
	$\mathbf{R_m}$		0.44	0.63	0.79	0.91	1.32	1.72	0.26
	$\mathbf{R_r}$		0.58	0.62	0.69	0.75	0.83	1.21	0.79
	$\mathbf{R_{rm}}$		0.15	0.19	0.24	0.29	0.45	0.65	0.10
	$\mathbf{R/R_{rm}}$		7.87	6.04	4.70	3.76	2.15	1.92	14.17
4 Antenna Phase Pattern	**R**	K/(°)	0.42	0.43	0.44	0.45	0.48	0.52	0.44
	$\mathbf{R_m}$		0.05	0.04	0.05	0.06	0.10	0.19	0.02
	$\mathbf{R_r}$		0.40	0.41	0.41	0.43	0.46	0.50	0.42
	$\mathbf{R_{rm}}$		0.02	0.02	0.03	0.04	0.08	0.16	0.01
	$\mathbf{R/R_{rm}}$		19.46	18.55	15.71	10.46	5.81	3.27	52.09
5 Channel Amplitude	**R**	K/(%)	0.34	0.35	0.35	0.32	0.28	0.32	0.39
	$\mathbf{R_m}$		0.13	0.12	0.16	0.24	0.37	0.50	0.05
	$\mathbf{R_r}$		0.17	0.19	0.19	0.20	0.21	0.29	0.21
	$\mathbf{R_{rm}}$		0.06	0.05	0.05	0.06	0.12	0.18	0.02
	$\mathbf{R/R_{rm}}$		6.08	7.34	6.65	4.94	2.35	1.78	19.23
6 Channel In phase	**R**	K/(°)	0.45	0.50	0.53	0.47	0.31	0.24	0.54
	$\mathbf{R_m}$		0.28	0.33	0.33	0.36	0.49	0.55	0.22
	$\mathbf{R_r}$		0.25	0.26	0.26	0.22	0.17	0.17	0.26
	$\mathbf{R_{rm}}$		0.04	0.07	0.07	0.06	0.15	0.24	0.02
	$\mathbf{R/R_{rm}}$		11.38	7.10	7.89	7.32	2.03	1.00	29.57
7 Channel Quadrature	**R**	K/(°)	0.22	0.23	0.25	0.25	0.23	0.27	0.27
	$\mathbf{R_m}$		0.15	0.15	0.15	0.16	0.23	0.29	0.12
	$\mathbf{R_r}$		0.14	0.15	0.17	0.19	0.21	0.27	0.18
	$\mathbf{R_{rm}}$		0.04	0.06	0.06	0.05	0.09	0.18	0.02
	$\mathbf{R/R_{rm}}$		5.92	4.21	4.14	4.82	2.51	1.55	11.23
8 Baseline Amplitude	**R**	K/(%)	0.20	0.21	0.21	0.20	0.16	0.13	0.23
	$\mathbf{R_m}$		0.07	0.07	0.09	0.14	0.23	0.32	0.04
	$\mathbf{R_r}$		0.11	0.11	0.12	0.12	0.12	0.11	0.12
	$\mathbf{R_{rm}}$		0.02	0.02	0.02	0.03	0.05	0.09	0.01
	$\mathbf{R/R_{rm}}$		9.00	10.29	8.59	5.92	3.18	1.50	17.06
9 Baseline Phase	**R**	K/(°)	0.28	0.29	0.32	0.32	0.27	0.24	0.34
	$\mathbf{R_m}$		0.19	0.20	0.21	0.22	0.29	0.33	0.15
	$\mathbf{R_r}$		0.20	0.20	0.21	0.21	0.19	0.19	0.22
	$\mathbf{R_{rm}}$		0.06	0.07	0.06	0.07	0.15	0.24	0.04
	$\mathbf{R/R_{rm}}$		4.52	4.34	5.38	4.84	1.77	1.02	9.12

[a]For each of the nine selected input errors, shown are the sensitivities **R** and $\mathbf{R_m}$ of $\langle \mathbf{a} \rangle$ and $\mathbf{s}(\mathbf{m})$ (no averaging whatsoever then area averaging) and the $\mathbf{R_r}$ and $\mathbf{R_{rm}}$ (same cases with preliminary averaging on redundant visibility samples). The $\mathbf{R/R_{rm}}$ ratio is the maximum reduction factor. These figures are computed for a 100 K uniform target and shown in successive columns for overlapping 200 km wide strips across the right half of the FOV as well as for the whole FOV.

out averaging redundant visibilities; the resulting sensitivities with and without area averaging are given on Table 2 as $\mathbf{R_m}$ and **R**, respectively. The $\mathbf{R/R_m}$ ratio is of the order of 1.5 on the average. The overall sensitivity gain factor when moving from **R** (neither area nor redundancies averages) to $\mathbf{R_{rm}}$ (both) is given as $\mathbf{R/R_{rm}}$ in the table. Values ranges from 8.6 to over 50.

[41] Figure 4 illustrates (from data in Table 2) the variation of all 4 sensitivities throughout the FOV, again for case 7. The **R** curve does not vary much; other sensitivities decrease (i.e., improve) strongly as one comes close to the middle strip. This is representative of the behavior of most sensitivities and most error cases, although a few exceptions can be seen on Table 2.

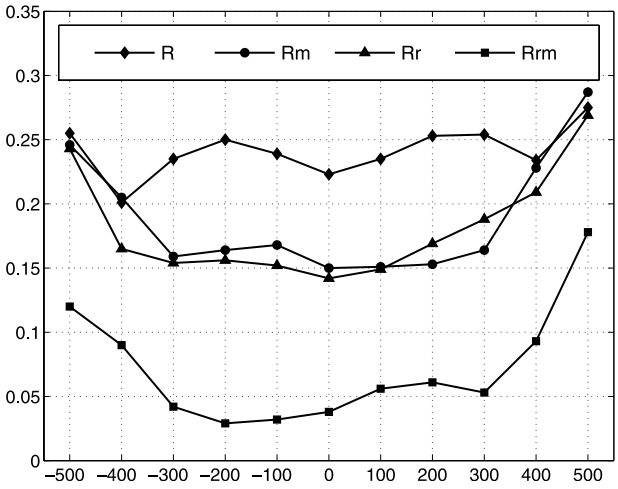


Figure 4. For error case 7, values of the four sensitivities **R, R_m, R_r,** and **R_{rm}** across the FOV, every 100 km, for overlapping strips 200 km wide. See color version of this figure at back of this issue.

[42] The summary of sensitivities over the whole FOV for all nine error cases is illustrated on Figure 5. The **R_m** and **R_{rm}** figures (area averaging) are always smaller than the corresponding values for any strip; this is not true for the **R** and **R_r** (redundancies alone) sensitivities. It is worth noting that the overall sensitivity improvement **R/R_{rm}** is always largest for the whole FOV, and always larger than the product **(R/R_r)** **(R_m/R_{rm})**; in other words, averaging redundant visibility samples reduces the spread of area averages more than it reduces the spread over FOV areas.

4. Application to the SMOS Mission and Conclusions

[43] This study shows that, due to the compounded effect of averaging first redundant visibilities and next brightness temperature errors over the whole FOV, the magnitude of instrument errors in 2-D interferometric radiometers may be decreased by a full order of magnitude.

[44] We have estimated a resulting error contribution, through using sensitivities **R_{rm}** and applying them to input errors which are representative of accuracies expected from the SMOS mission characteristics, accounting for the on board calibration system [*Corbella et al.*, 2000a, 2000b]. Results are shown on Table 3.

[45] It has been verified in the simulations that the variances for individual errors could be approximately summed up. The overall resulting standard deviation (see bottom of table) is then found to be 0.043 K for the whole FOV.

[46] This figure is neither an accurate nor an exhaustive estimate of instrument errors for ocean measurements by SMOS. Concerning antennas, the estimated contributions correspond to generic error modeling choices, whereas measurements on antenna prototypes [*Camps et al.*, 1997b] suggest more specific uncertainties, described as amplitude and phase ripples. Furthermore, instrument errors may have to be modulated depending on the amplitude and monitoring accuracy of thermal and mechanical effects during the flight. Concerning receiver and baseline errors, estimated residual contributions should be compounded with short-term instabilities or variations between calibration sequences, in principle scheduled every orbit. Several significant error sources such as the offset of correlators have been ignored.

[47] On the other hand, additional interferometer elements at the back of each antenna arm, included in the SMOS design, may be expected to improve the efficiency of averaging redundant visibility samples.

[48] Finally, a rigorous assessment will have to reproduce the aggregation of individual retrievals, for which brightness temperature data are selected along dwell lines within the geographical FOV [*Waldteufel et al.*, 2003]. All these steps need further developments.

[49] Over a given ocean area, successive orbits during a 10-day period will allow the radiometer to sample quasi randomly various strips across the FOV. This does accomplish piecewise FOV averaging as far as instrument errors are concerned. On the equator, considering only the morning orbits, a 10-day period allows to sample about 72% of the total swath; therefore the efficiency of area averaging will be smaller than indicated above. At higher latitudes however, and/or if both morning and evening orbits are considered, the swath coverage over every space/time averaging domain will

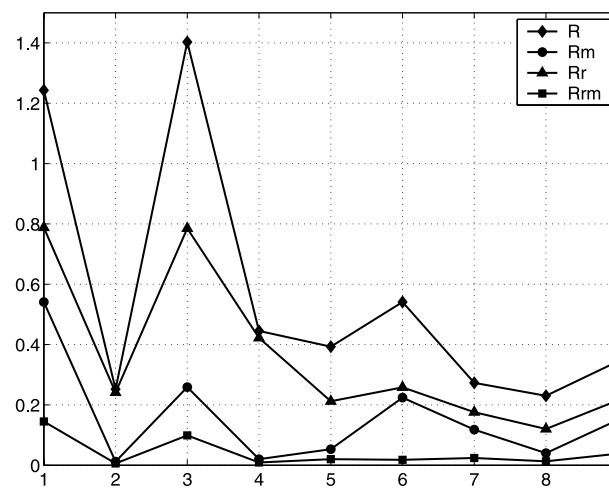


Figure 5. For the nine error cases, plot of the four sensitivities **R, R_m, R_r, and R_{rm}** over the whole FOV. See color version of this figure at back of this issue.

Table 3. Application to SMOS[a]

Case	Error Size	Unit	Limits Across FOV (×100 km)						Whole FOV
			(−1,1)	(0,2)	(1,3)	(2,4)	(3,5)	(4,6)	
1	0.10	K/(°)	0.042	0.032	0.021	0.046	0.082	0.094	0.015
2	0.60	K/(%)	0.008	0.010	0.010	0.017	0.030	0.055	0.004
3	0.05	K/(°)	0.007	0.010	0.012	0.014	0.023	0.033	0.005
4	0.33	K/(°)	0.007	0.008	0.009	0.014	0.027	0.053	0.003
5	0.60	K/(%)	0.033	0.029	0.031	0.038	0.073	0.109	0.012
6	0.60	K/(°)	0.024	0.042	0.040	0.039	0.090	0.142	0.011
7	0.20	K/(°)	0.008	0.011	0.012	0.011	0.019	0.036	0.005
8	1.50	K/(%)	0.033	0.030	0.037	0.050	0.078	0.129	0.020
9	0.80	K/(°)	0.049	0.054	0.047	0.052	0.121	0.189	0.030
All			0.085	0.089	0.084	0.105	0.208	0.319	0.043

[a]For input error magnitudes (shown in the second column) representative of SMOS expected performances over oceans, a resulting error is finally estimated using the $\mathbf{R_{rm}}$ sensitivity. Other features are similar to those in Table 2.

exceed 100%; additional reduction of the effect of some instrument errors may then be hoped for.

[50] The reduction factors identified in this study suggest that the overall resulting accuracy of salinity measurements by SMOS may well be ultimately dictated, rather than by interferometer errors, by geophysical errors (e.g., surface wind) and by the quality of the overall brightness temperature calibration.

[51] **Acknowledgments.** This work was supported by the Centre National de la Recherche Scientifique (CNRS), Centre National d'Etudes Spatiales (CNES), and Région Midi-Pyrénées. ESA supported the 2-D interferometer studies within the MIRAS Demonstrator Pilot Project. Computing facilities were provided by CERFACS. Fruitful exchanges with I. Corbella, C. Cot, and M. Martin Neira are acknowledged.

References

Bara, J., A. Camps, F. Torres, and I. Corbella, Angular resolution of two-dimensional hexagonally sampled interferometric radiometers, *Radio Sci.*, *33*(5), 1459–1473, 1998.

Camps, A., Application of interferometric radiometry to Earth observation, Ph.D. thesis, Univ. Politech. de Catalunya, Barcelona, Spain, 1996.

Camps, A., J. Bara, I. Corbella, and F. Torres, The processing of hexagonally sampled signals with standard rectangular techniques: Application to 2D large aperture synthesis interferometric radiometers, *IEEE Trans. Geosci. Remote Sens.*, *35*(1), 183–189, 1997a.

Camps, A., J. Bara, F. Torres, I. Corbella, and J. Romeau, Impact of antenna errors on the radiometric accuracy of large aperture synthesis radiometers, *Radio Sci.*, *32*(2), 657–668, 1997b.

Corbella, I., A. Camps, and F. Torres, Analysis of noise-injection networks for interferometric radiometer calibration, *IEEE Trans. Microwave Theory Tech.*, *48*(4), 545–552, 2000a.

Corbella, I., F. Torres, A. Camps, J. Bara, M. Vall-llosera, and N. Duffo, L-band aperture synthesis microwave radiometry: Hardware requirements and system performance, in *Proceedings of IGARSS'2000, Hawaii, USA*, pp. 2975–2977, Inst. of Electr. and Electron. Eng., Bellingham, Wash., 2000b.

Kerr, Y. H., P. Waldteufel, J. P. Wigneron, J. M. Martinuzzi, J. Font, and M. Berger, Soil moisture retrieval from space: The Soil Moisture and Ocean Salinity (SMOS) Mission, *IEEE Trans. Geosci. Remote Sens.*, *39*(8), 1729–1735, 2001.

Lannes, A., and E. Anterrieu, Image reconstruction methods for remote sensing by aperture synthesis, in *Proceedings of IGARSS'94, Pasadena, USA*, pp. 2892–2903, Inst. of Electr. and Electron. Eng., Bellingham, Wash., 1994.

Ruf, C. S., C. T. Swift, A. B. Tanner, and D. M. LeVine, Interferometric synthetic aperture radiometry for the remote sensing of the Earth, *IEEE Trans. Geosci. Remote Sens.*, *26*(5), 597–611, 1998.

Torres, F., A. Camps, J. Bara, I. Corbella, and R. Ferrero, On board phase and modulus calibration of large aperture synthesis radiometers: Study applied to Miras, *IEEE Trans. Geosci. Remote Sens.*, *35*(4), 1000–1009, 1996.

Torres, F., A. Camps, J. Bara, and I. Corbella, Impact of receiver errors on the radiometric resolution of large two-dimensional aperture synthesis radiometers, *Radio Sci.*, *32*(2), 629–641, 1997.

Waldteufel, P., and G. Caudal, About off-axis radiometric polarimetric measurements, *IEEE Trans. Geosci. Remote Sens.*, *40*(6), 1435–1439, 2002.

Waldteufel, P., J. Boutin, and Y. H. Kerr, Selecting an optimal configuration for the SMOS mission, *Radio Sci.*, *38*, doi:10.1029/2002RS002744, in press, 2003.

E. Anterrieu, CERFACS, Signal and Image Processing, 42 avenue Gaspard Coriolis, F-31057 Toulouse, France. (Eric.Anterrieu@cerfacs.fr)

G. Caudal, IPSL, Centre d'Etude des Environnements Terrestre et Planétaires, 10-12 avenue de l'Europe, F-78140 Vélizy, France.

P. Waldteufel, IPSL, Service d'Aéronomie du Centre National de la Recherche Scientifique (CNRS), B.P. 3, F-91371 Verrières le Buisson, France.

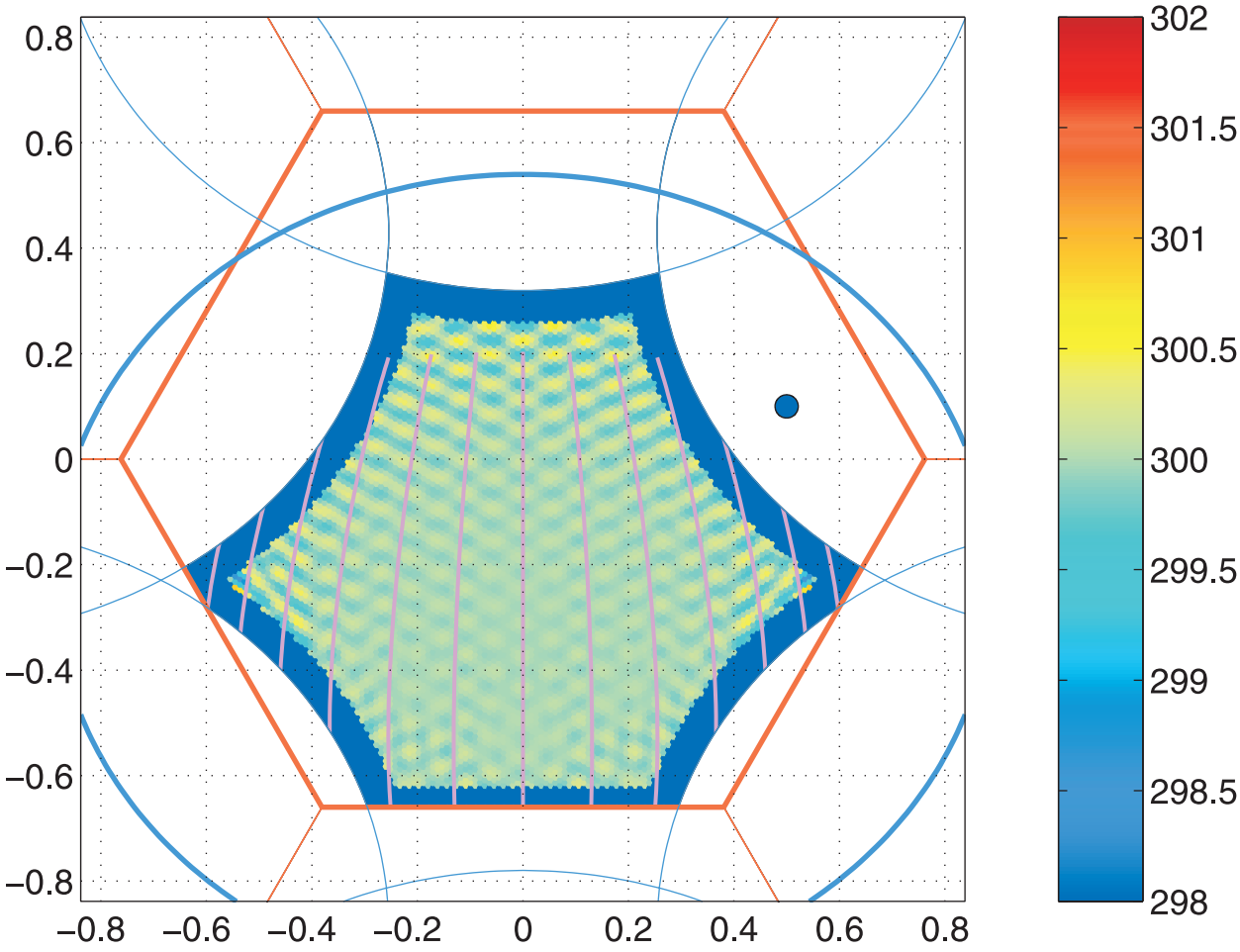


Figure 1. (a) Reconstructed image of a 300 K homogeneous target in the SMOS FOV showing Gibbs oscillations, for a 30° tilting angle of the antenna plane and a 30° steering angle of the Y-shaped interferometer, in the frame of direction cosines. The alias-free FOV is limited by replicas of the Earth horizon (blue ellipses). Also shown are the margins applied to the reconstruction zone and the limits between dwell lines for building the statistics (magenta lines are spaced 100 km apart). The width of the margins is 1.5 times the resolution provided by the half maximum Blackman window in the direction cosine frame (shown as a blue circle in the upper right part of the figure). (b) Histograms of the discretization error (K) for different dwell lines (violet) and for the whole FOV (green). In each case, the mean area bias and the area spread **m** and **a** are depicted (see text).

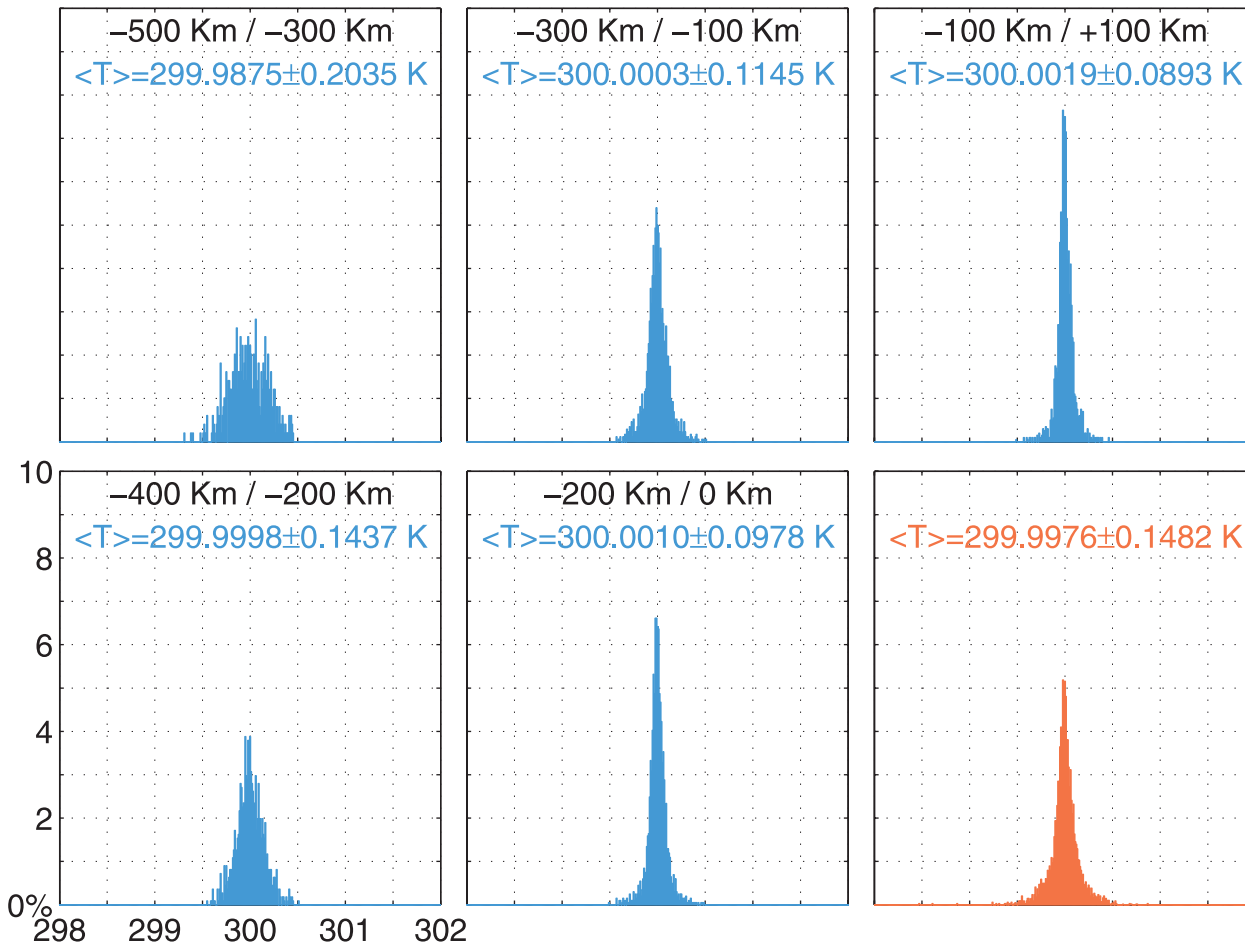


Figure 1. (continued)

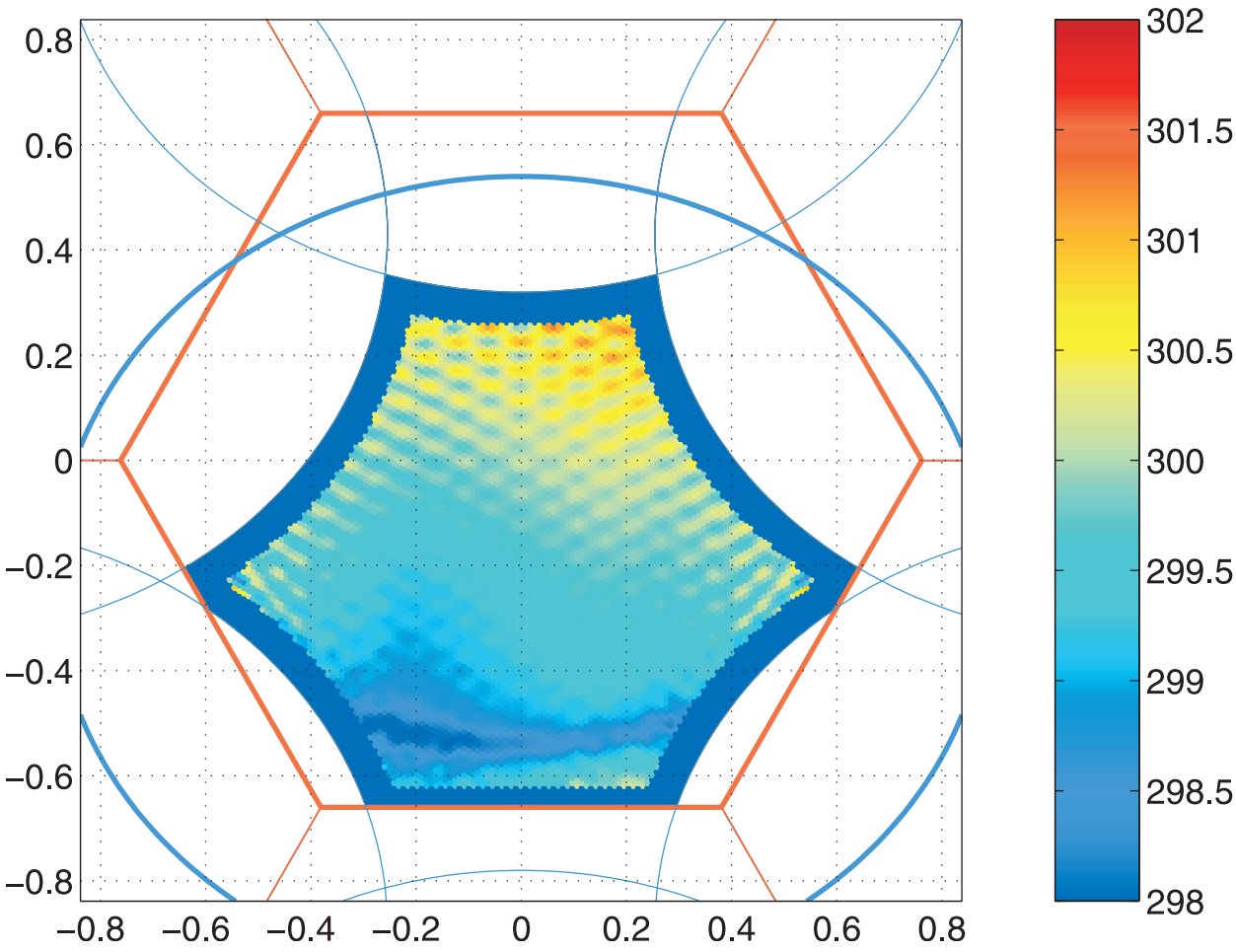


Figure 2. Same as Figure 1 when introducing a uniform 0.5° error on quadratic phases in the receiving channels (error case 7).

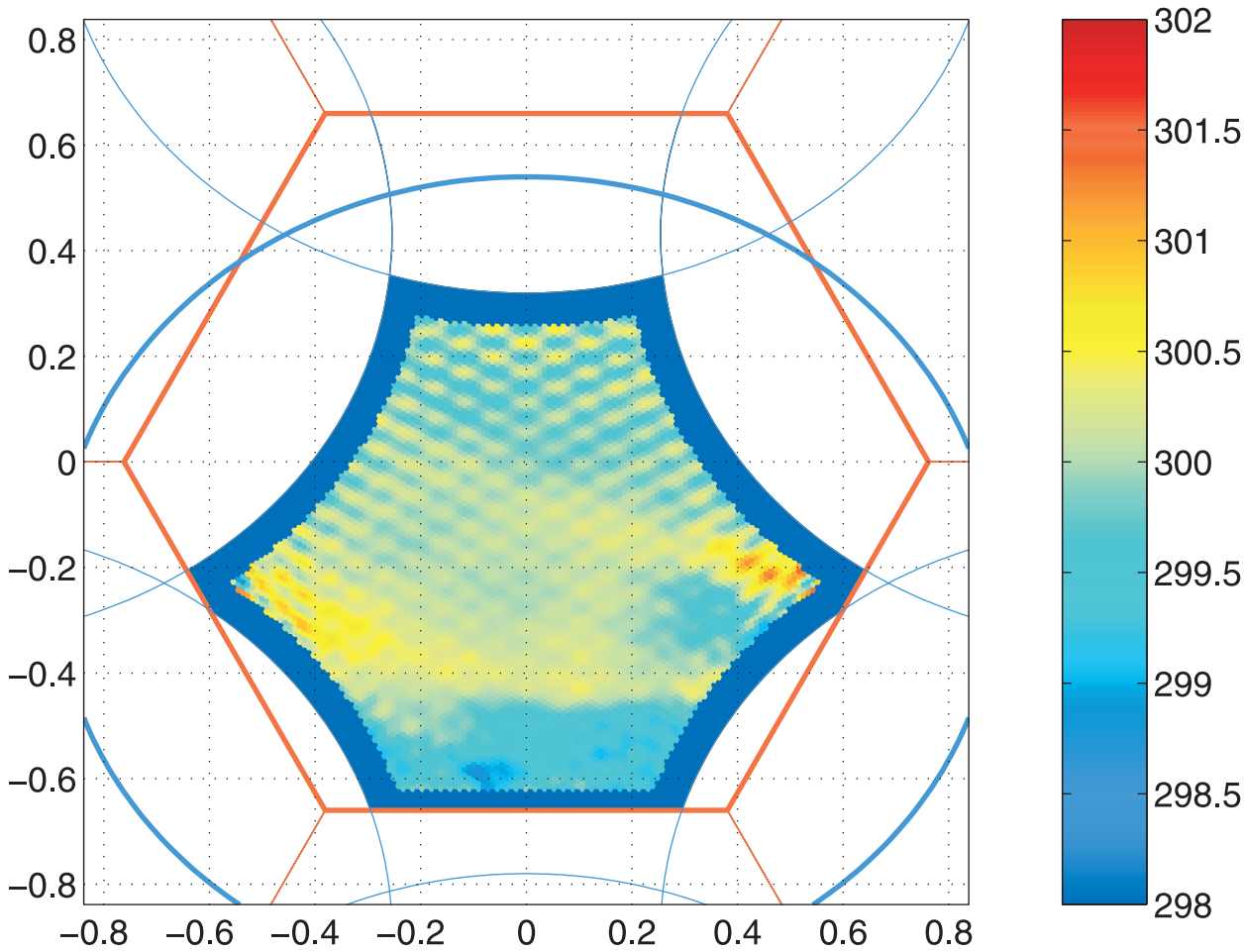


Figure 3. Errors on the reconstructed field when introducing a Gaussian distributed error with a 0.5° standard deviation on quadratic phases in the receiving channels (error case 7). (a) Example of reconstructed image, to be compared to Figure 2 (whole FOV) and (b) histogram of error values mapped on (a) (top part). The bottom part shows the successive values taken by **m** and **a** on the whole FOV when repeating the numerical experiment 100 times. The diagrams also display the building up of ensemble standard deviations **s(m)** and **s(a)** and show the resulting ensemble averages.

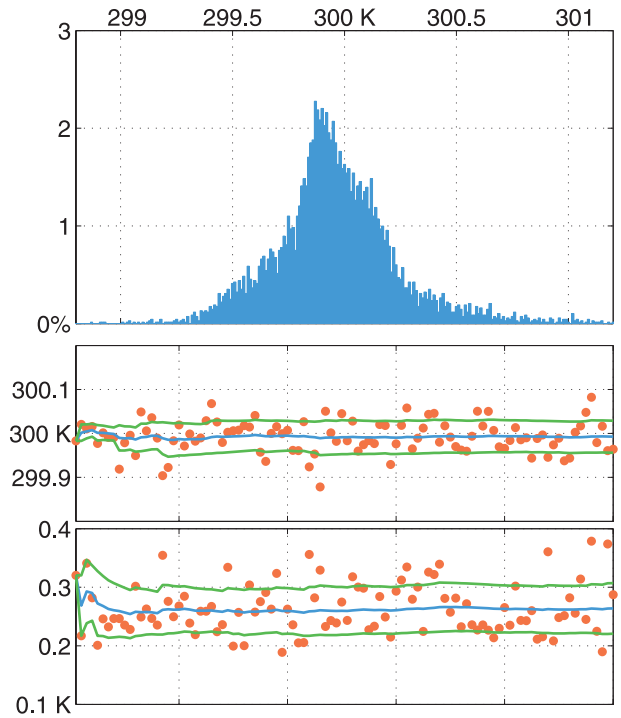


Figure 3. (continued)

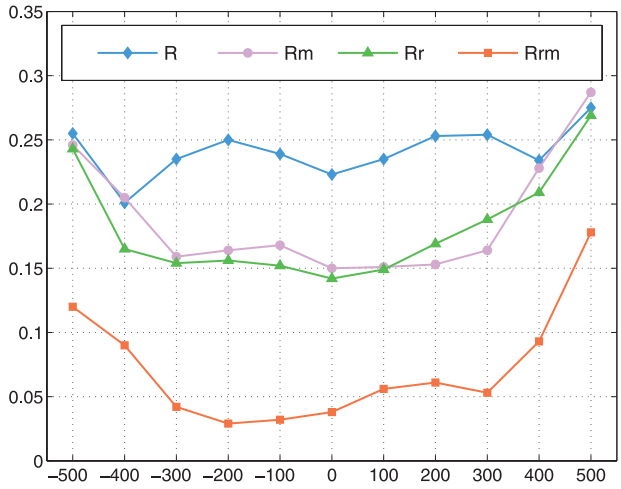


Figure 4. For error case 7, values of the four sensitivities **R, R_m, R_r, and R_{rm}** across the FOV, every 100 km, for overlapping strips 200 km wide.

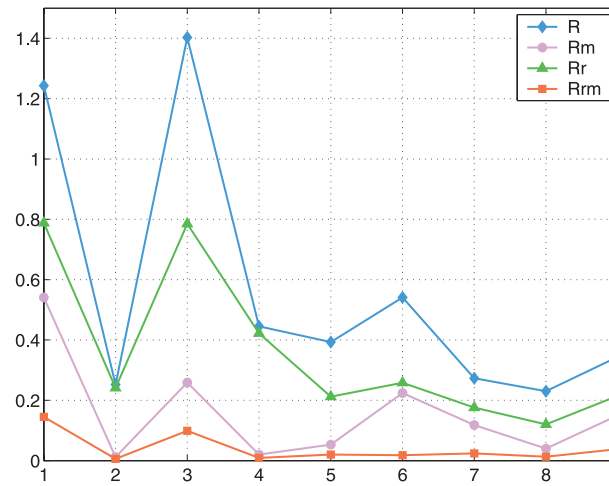


Figure 5. For the nine error cases, plot of the four sensitivities **R, R_m, R_r, and R_{rm}** over the whole FOV.